

Anomalous Radio-Wave Scattering from Interstellar Plasma Structures

J. M. Cordes

Astronomy Department and NAIC, Cornell University; cordes@spacenet.tn.cornell.edu

T. Joseph W. Lazio

Code 7213, Naval Research Laboratory, Washington, DC 20375-5351; lazio@rsd.nrl.navy.mil

ABSTRACT

This paper considers scattering screens that have arbitrary spatial variations of scattering strength transverse to the line of sight, including screens that are spatially well confined, such as disks and filaments. We calculate the scattered image of a point source and the observed pulse shape of a scattered impulse. The consequences of screen confinement include: (1) Source image shapes that are determined by the physical extent of the screen rather than by the shapes of much-smaller diffracting microirregularities. These include image elongations and orientations that are frequency dependent. (2) variation with frequency of angular broadening that is much weaker than the trademark ν^{-2} scaling law, including frequency-independent cases; and (3) similar departure of the pulse broadening time from the usually expected ν^{-4} scaling law. Applications include scattering of pulses from the Crab pulsar by filaments in the Crab Nebula; image asymmetries from Galactic scattering of the sources Cyg X-3, Sgr A*, and NGC 6334B; and scattering of background active galactic nuclei by intervening galaxies. We also address the consequences for inferences about the shape of the wavenumber spectrum of electron density irregularities, which depend on scaling laws for the image size and the pulse broadening. Future low-frequency (< 100 MHz) array observations will also be strongly affected by the Galactic structure of scattering material. Our formalism is derived in the context of radio scattering by plasma density fluctuations. It is also applicable to optical, UV and X-ray scattering by grains in the interstellar medium.

Subject headings: ISM: structure — pulsars: general — scattering

1. Introduction

Images of scattered radio sources and distorted pulses from pulsars provide some of the most-used observables for probing microstructure in the electron density of interstellar gas. Over the last decade, interstellar scattering measurements have revealed asymmetries in the scattered images of radio sources. These are most often interpreted in terms of underlying anisotropy of the very small irregularities that diffract the radiation. That anisotropy, in turn, most likely reflects the

orientation of magnetic fields in the H II gas that contains the microstructure. Angular broadening of compact sources and pulse distortions due to multipath propagation are used to probe the amplitude of scattering and also, through the frequency scaling, to constrain the shape of the wavenumber spectrum for the microstructure. Inversion of scattering observables into information about the microstructure almost invariably relies on the assumption that the scattering strength is uniform in directions transverse to the line of sight.

We reconsider the assumptions used to analyze angular and temporal broadening, in particular the assumption of uniformity across the line of sight. One reason is that the interstellar medium (ISM) shows structures on a wide variety of scales and so it is unreasonable to expect the scattering to be uniform across all lines of sight. Secondly, the physics that underlies asymmetric images is quite different if the asymmetry occurs on scales larger than diffractive scales. Thirdly, observations of the Crab pulsar show anomalous scalings of pulse broadening with frequency. These are interpreted by some as indicating that scattering occurs within the pulsar magnetosphere rather than in a cold plasma (J. Eilek 1997, private communication; Hankins & Moffett 1998; Lyutikov & Parikh 2000). As we show, anomalous scalings occur quite naturally from cold plasma extrinsic to the pulsar if the scattering region is bounded in the transverse direction. Additionally, future observations at low radio frequencies of a variety of sources—including high redshift sources—are expected to reveal further anomalous scattering that most likely will be the result of confined scattering structures. Finally, the scaling with frequency of angular and pulse broadening is often used to constrain the shape of the wavenumber spectrum of scattering irregularities (e.g., Cordes, Weisberg, & Boriakoff 1985; Fey et al. 1991). Weakening of the frequency dependence by confined plasma structures would be interpreted as a steeper wavenumber spectrum. Thus it is important to assess the role of confined structures in the observations of scattered radio sources.

In §2 we discuss previous treatments of angular and pulse broadening. In §3 we derive a general formalism for scattering that takes into account arbitrary variations of scattering strength transverse to the line of sight. Examples are given in §4. Applications to the Crab pulsar and other Galactic sources are given in §5. Future observations of extragalactic sources and at low frequencies are considered in §6. In §7 we discuss possible implications for the interstellar medium. Finally, in §8, we summarize our results.

2. Past Treatments of Angular & Pulse Broadening

It is well known that the shape of a scattered impulse, viewed through a thin, infinitely-extended screen with a circularly symmetric, Gaussian angle distribution, is a one-sided exponential (e.g., Rickett 1990 and references therein). Thick scattering screens produce slower rise times, while screens containing Kolmogorov irregularities (e.g., Rickett 1990; Lambert & Rickett 1999) produce decays that are slower than exponential. Results along these lines have been presented by Scheuer (1968), Williamson (1972, 1973, 1975), Lee & Jokipii (1975), and Isaacman & Rankin (1977). Williamson (1975) has shown that the pulse broadening function from multiple,

discrete screens or from a continuous medium consists of an n -fold convolution of (one-sided) exponential functions. Williamson’s result applies to the case where the phase structure function is square-law in form. Media with Kolmogorov wavenumber spectra produce different shapes, though the differences are small compared to effects we consider in this paper. The key, implicit assumption in Williamson’s analysis (and essentially all other published results on interstellar pulse broadening; however, see Lyne & Thorne 1975) is that the transverse extent of the scattering screen is arbitrarily large. If this assumption is relaxed, quite different results emerge.

We show that several “anomalous” phenomena occur when scattering structures have finite transverse extent, including:

1. Angular broadening from scattering or refraction that scales anomalously with ν . In the case of radio scattering in cold plasmas, anomalous scaling is defined as a significant departure from a ν^{-2} scaling, which is determined by the microphysics of the plasma.¹ Departures will always consist of a *weaker* dependence on frequency.
2. Elongated (or otherwise distorted) images of point sources that are due to scattering but do not scale as ν^{-2} .
3. Multiple imaging by screens, with image intensities influenced by focusing (curvature of the screen phase) and by dilution from scattering.
4. Temporal broadening of pulsar pulses which shows a *weaker* dependence on frequency than ν^{-4} , in accord with the scaling of angular broadening.²
5. Replication of pulses by multiple imaging from an ensemble of screens.

3. Probability Densities for Angle of Arrival & Time of Arrival

We derive the image of a scattered point source and the scattered pulse shape of an impulse by calculating the probability density functions (PDFs) for the angle of arrival and the time of arrival, respectively.

Consider a series of diffracting screens at distances D_{sj} from a source at distance D from the observer. Letting \mathbf{a}_j be the (two-dimensional) scattering angle from the j th screen, the angular deviation $\theta(s)$ of a ray path and its transverse offset $\mathbf{x}(s)$ from the direct ray path at distance s

¹Scattering from irregularities with a Kolmogorov wavenumber spectrum shows $\nu^{-11/5}$ scaling under the circumstance of moderate scattering (cf. Cordes & Lazio 1991). We do not consider this scaling anomalous. When a confined structure contains Kolmogorov fluctuations, the scaling of angular size will be shallower than $\nu^{-11/5}$.

²A Kolmogorov spectrum can show a $\nu^{-22/5}$ scaling for pulse broadening. As with angular broadening, we do not consider this anomalous.

from the source are

$$\boldsymbol{\theta}(s) = \boldsymbol{\theta}_i + \sum_j \mathbf{a}_j U(s - D_{sj}) \quad (1)$$

$$\mathbf{x}(s) = s\boldsymbol{\theta}_i + \sum_j (s - D_{sj})\mathbf{a}_j U(s - D_{sj}), \quad (2)$$

where $U(x)$ is the unit step function. The first equation relates the observed ray angle ($\boldsymbol{\theta}$) to the initial ray angle ($\boldsymbol{\theta}_i$) and the scattering angles (\mathbf{a}_j). The relation $\mathbf{x}(D) = 0$ stipulates that rays must reach the observer. We assume all angles are small ($|\boldsymbol{\theta}_i|, |\mathbf{a}_j|, |\boldsymbol{\theta}| \ll 1$), though it is not difficult to extend our results to large angles. Including only the geometric path-length difference, the corresponding time delay relative to the direct ray path is

$$t = \frac{1}{2c} \int_0^D ds |\boldsymbol{\theta}(s)|^2. \quad (3)$$

The overall time delay also includes a dispersive component, but this is unlikely to differ significantly across an individual screen. However, as we explore elsewhere, differential dispersion between screens is likely to be important.

To calculate the probability density function (PDF) of the observed angle of arrival (AOA), $\boldsymbol{\theta}$, and time of arrival (TOA), t , we use Dirac delta functions to enforce Eq. 1 and $\mathbf{x}(D) = 0$ for those rays that reach the observer. We use conditional probabilities to include these relations and to integrate over the PDFs for the scattering angles in each screen and over the PDF of $\boldsymbol{\theta}_i$. The result is simple for an isotropic source or, less restrictively, where the PDF of $\boldsymbol{\theta}_i$ is constant over the relevant range of initial ray angles, $\boldsymbol{\theta}_i$.

It is standard to assume the scattering strength is invariant across a scattering screen. Here we specify a more general description. Consider each screen to scatter or refract rays according to a PDF $f_{\mathbf{a}_j}$ whose width varies arbitrarily across the screen. Accordingly we write each screen's PDF as $f_{\mathbf{a}_j}(\mathbf{a}_j; \mathbf{x}(D_{sj}))$, where $\mathbf{x}(D_{sj})$ is Eq. 2 evaluated at the location of each screen, $s = D_{sj}$.

Let Q be an observed quantity such as the AOA or TOA and let $Q'(\mathbf{a}_j, D_{sj}, D)$ be its value given \mathbf{a}_j and D_{sj} . The PDF of Q is

$$f_Q(Q) = \frac{\prod_j \int d\mathbf{a}_j f_{\mathbf{a}_j}(\mathbf{a}_j; \mathbf{x}(D_{sj})) \delta(\mathbf{x}(D)) \delta(Q - Q'(\mathbf{a}_j, D_{sj}, D))}{\prod_j \int d\mathbf{a}_j f_{\mathbf{a}_j}(\mathbf{a}_j; \mathbf{x}(D_{sj})) \delta(\mathbf{x}(D))}, \quad (4)$$

where the numerator is the joint PDF of Q and $\mathbf{x}(D) = 0$ (that rays reach the observer), while the denominator is the probability that rays reach the observer.

3.1. The General Single Screen (N=1)

For the simple case of a single scattering screen, Eq. 4 becomes

$$f_Q(Q) = \frac{\int d\mathbf{a} f_{\mathbf{a}}(\mathbf{a}; -\mathbf{a}D_s') \delta(Q - Q'(\mathbf{a}, D_s, D))}{\int d\mathbf{a} f_{\mathbf{a}}(\mathbf{a}; -\mathbf{a}D_s')}, \quad (5)$$

where

$$D_s' = D_s(1 - D_s/D). \quad (6)$$

For the angle of arrival, $Q = \theta$, $Q' = \mathbf{a}(D_s/D)$ and

$$f_{\theta}(\theta) = \left(\frac{D}{D_s}\right)^2 \frac{f_{\mathbf{a}}\left(\frac{D}{D_s}\theta; -\theta(D - D_s)\right)}{\int d\mathbf{a} f_{\mathbf{a}}(\mathbf{a}; -\mathbf{a}D_s')}. \quad (7)$$

For the TOA, $Q = t$ and $Q' = D_s(1 - D_s/D)|\mathbf{a}|^2/2c$ so only the magnitude, $|\mathbf{a}|$, is constrained. Transformation of $\delta(Q - Q')$ to $\delta(|\mathbf{a}| - a_t)$ yields

$$f_t(t) = \left(\frac{c}{D_s'}\right) \frac{\int_0^{2\pi} d\phi f_{\mathbf{a}}(a_t \hat{\mathbf{a}}_\phi; -a_t \hat{\mathbf{a}}_\phi D_s')}{\int d\mathbf{a} f_{\mathbf{a}}(\mathbf{a}; -\mathbf{a}D_s')}, \quad (8)$$

where $\hat{\mathbf{a}}_\phi$ is a unit vector,

$$\hat{\mathbf{a}}_\phi = \cos \phi \hat{\mathbf{x}} + \sin \phi \hat{\mathbf{y}}, \quad (9)$$

and

$$a_t = \left(\frac{2ct}{D_s'}\right)^{1/2}. \quad (10)$$

The flux density of a source is conserved only for an infinite screen with homogeneous statistics because only in that case is as much flux scattered toward the observer as is scattered away. We define the flux dilution factor as the ratio of the probability that rays reach the observer to the probability for a uniform, infinite screen:

$$\eta_F = \int d\mathbf{a} f_{\mathbf{a}}(\mathbf{a}; -\mathbf{a}D_s'), \quad (11)$$

equal to the denominator of Eq. 5. For a uniform, infinite screen, $\eta_F = 1$. In general, $\eta_F \leq 1$.

We illustrate these expressions by considering specific cases.

3.1.1. Infinitely Wide Screen with Homogeneous Statistics

For an infinite screen with homogeneous statistics, the denominator of Eq. 5 is unity. Specializing to circularly symmetric $f_{\mathbf{a}}$, we find the normalized 1D PDF for the magnitude $\theta \equiv |\boldsymbol{\theta}|$:

$$f_{\theta}(\theta) = 2\pi\theta \left(\frac{D}{D_s}\right)^2 f_{\mathbf{a}}(D\theta/D_s). \quad (12)$$

If $f_{\mathbf{a}}$ is a Gaussian function with rms angle σ_a in each coordinate direction, then

$$f_{\theta}(\theta) \approx \sigma_{\theta}^{-2} \theta e^{-\theta^2/2\sigma_{\theta}^2} \quad (13)$$

$$\sigma_{\theta} \equiv (D_s/D)\sigma_a \quad (14)$$

$$f_t(t) = \tau_0^{-1} e^{-t/\tau_0} U(t) \quad (15)$$

$$\tau_0 = D_s' \sigma_a^2 / c. \quad (16)$$

The 1D rms angle

$$\theta_{\text{rms}} \equiv \frac{1}{\sqrt{2}} \langle |\boldsymbol{\theta}|^2 \rangle^{1/2} \quad (17)$$

characterizes the *observed* range of angles and in this case is identical to σ_{θ} , which is the scaled range of *scattering* angles. In general, $\theta_{\text{rms}} \neq \sigma_{\theta}$.

If $\sigma_a \propto \nu^{-2}$ as for a plasma, then the AOA PDF has a scale $\sigma_{\theta} \propto \nu^{-2}$ and the TOA PDF has scale $\tau_0 \propto \nu^{-4}$. These scaling laws for observable quantities rely on the assumption that the screen is infinitely wide.

3.1.2. Circular Screen with Finite Radius

Consider a circular screen with radius X_{max} centered on the line of sight. Now the PDF for θ is truncated for $\theta > \theta_{\text{max}} \equiv X_{\text{max}}/(D - D_s)$. Again adopting circularly symmetric, Gaussian statistics for \mathbf{a} , we find

$$f_{\theta}(\theta) = [\sigma_{\theta}^2(1 - e^{-\zeta})]^{-1} \theta e^{-\theta^2/2\sigma_{\theta}^2} U(\theta_{\text{max}} - \theta), \quad (18)$$

$$\zeta \equiv \frac{1}{2} \left(\frac{\theta_{\text{max}}}{\sigma_{\theta}} \right)^2, \quad (19)$$

where the unit step function enforces truncation of the PDF for $\theta > \theta_{\text{max}}$. If the rms scattering angle is small, $\sigma_a \ll X_{\text{max}}D/(D_s(D - D_s))$, the scaling of the observed size with wavelength is according to that of σ_a . For larger refraction angles, the physical size of the screen becomes important. To see this, we calculate the rms angular size, which is, for the circularly symmetric Gaussian and a wavelength scaling $\sigma_a = \sigma_{a0}(\nu/\nu_0)^{-2}$,

$$\theta_{\text{rms}} = \sigma_{a0} \left(\frac{D_s}{D} \right) \left(\frac{\nu}{\nu_0} \right)^{-2} \left[\frac{1 - (1 + \zeta)e^{-\zeta}}{1 - e^{-\zeta}} \right]^{1/2}. \quad (20)$$

The wavelength scaling is $\zeta \propto \nu^4$. At large ν , $\zeta \gg 1$ and $\theta_{\text{rms}} \propto \nu^{-2}$. At small ν , $\zeta \rightarrow 0$ and θ_{rms} becomes frequency independent.

The TOA has a PDF and mean value

$$f_t(t) = \frac{e^{-t/\tau_0}}{\tau_0(1-e^{-\zeta})} U(t_{\text{max}} - t) \quad (21)$$

$$\langle t \rangle = \tau_0 \left[1 - \zeta \left(\frac{e^{-\zeta}}{1-e^{-\zeta}} \right) \right] \quad (22)$$

$$t_{\text{max}} = \zeta \tau_0. \quad (23)$$

For a wide screen, $\zeta \rightarrow \infty$, $t_{\text{max}} \rightarrow \infty$ and $\langle t \rangle = \tau_0$, as before. However, a narrow screen with $\zeta \ll 1$ gives $\langle t \rangle \sim \zeta \tau_0$.

The observed flux of a source viewed through the truncated screen is attenuated by the scattering. The flux dilution factor is

$$\eta_F = 1 - e^{-\zeta}. \quad (24)$$

For $\zeta \ll 1$, $\eta_F \sim \zeta$ while $\zeta \gg 1$ yields $\eta_F = 1$. When the angular diameter and pulse broadening of a source are observed to have anomalous wavelength dependence, ie. when scattering is dominated by a truncated screen, the flux is diminished. Inspection of Eq. 20 and Eq. 24 indicates that there can be a correlation of rms angular size and flux density.

3.2. A Screen with Arbitrary Variations of Scattering Strength

Above, we considered screens with extreme variations of scattering strength: discontinuous or truncated to zero. Here we consider other cases that may have relevance to sources that are viewed through scattering regions with structure on scales $\sim (D - D_s)\theta$. As in Eq. 4, we specify the scattering angle \mathbf{a}_j from the j th screen by a PDF that depends on location along the screen, $\mathbf{x}(D_{s_j})$: $f_{\mathbf{a}_j}(\mathbf{a}_j; \mathbf{x}(D_{s_j}))$. For simplicity, we drop the j subscripts and discuss scattering from a single screen. Also, for ease of discussion, we consider $f_{\mathbf{a}}$ to be a 2D Gaussian with angular variance $\sigma_{\mathbf{a}}(\mathbf{x})$ that varies across the screen.

In some circumstances, the angle-of-arrival distribution $f_{\boldsymbol{\theta}}$ is determined purely by the shape and width of $f_{\mathbf{a}}$, while in others it is determined by the variations in $\sigma_{\mathbf{a}}$ across the screen. If $\sigma_{\mathbf{a}}$ is constant across the screen, $f_{\boldsymbol{\theta}}$ is a scaled version of $f_{\mathbf{a}}$ and the wavelength scaling of the observed angular size is identical to that of the scattering angles.

However, if $\sigma_{\mathbf{a}}$ varies across the screen, the observed angular size may reflect variations of $\sigma_{\mathbf{a}}$ in addition to or rather than the width of $f_{\mathbf{a}}$ itself. Let $\ell_{\mathbf{a}}$ be the characteristic length scale on which $\sigma_{\mathbf{a}}$ varies across the screen. We compare this with the observed angular diameter projected back to the screen, yielding a length scale $\ell_{\perp} \sim (D - D_s)\theta_{\text{rms}}$. We consider three cases:

1. If $\ell_{\mathbf{a}} \ll \ell_{\perp}$ and variations in $\sigma_{\mathbf{a}}$ are statistically homogenous, the variations average out. The scaling with wavelength of the observed AOA width is identical to that of \mathbf{a} , which is due to the microphysics.
2. If $\ell_{\mathbf{a}} \gg \ell_{\perp}$, then $\sigma_{\mathbf{a}} \approx$ constant over the part of the screen sampled and the angle-of-arrival PDF is determined by $f_{\mathbf{a}}$. The wavelength scaling is again determined by the microphysics. Depending on how large $\ell_{\mathbf{a}}$ is, eventually time variations in the image are expected on a time scale $t_a \sim \ell_{\mathbf{a}}/V_{\text{eff}}$, where V_{eff} is an effective velocity determined by the velocities of the source, medium and observer (e.g., Cordes & Rickett 1998).
3. If $\ell_{\mathbf{a}} \sim \ell_{\perp}$, the AOA PDF is determined by a combination of $f_{\mathbf{a}}$ and the spatial variation of $\sigma_{\mathbf{a}}$. The truncated screen of §3.1.2 is an extreme example of this case. The wavelength scaling is likely to depart significantly from that of the microphysics.

4. Examples

4.1. Illustration of Anomalous Frequency Scaling

Figure 1 shows the “image” $f_{\boldsymbol{\theta}}$, the pulse broadening function f_t , and the scaling with frequency of the pulse broadening time for two cases: (a) an infinite screen (bold solid lines) and (b) a truncated circular screen centered on the direct line of sight (light and dashed lines). The underlying scattering function ($f_{\mathbf{a}}$) is a circular Gaussian PDF, and the rms scattering angle scales as ν^{-2} . For the infinite screen, the pulse broadening scales as ν^{-4} , as expected. However, the truncated screen yields truncated images and truncated pulse broadening functions if the rms scattering angle is large enough that rays from the screen’s edges reach the observer. Thus, truncation occurs at low frequencies and not at high frequencies. For the example given, the break frequency ~ 0.5 GHz. Actual break frequencies will depend on particular sizes and scattering strengths of screens.

As a second illustration of anomalous frequency scaling, we calculate the pulse broadening for a pulse scattered by a two component screen. The first, circular component with radius X_1 is centered on the line of sight and scatters radiation much more strongly than the remainder of the screen, which is of infinite extent. The distributions of AOA and TOA follow from the master equations, Eq. 7,8. The rms angular size, the mean TOA, and related quantities are:

$$\theta_{\text{rms}} = \sqrt{2} \sigma_{d1} \left(\frac{D_s}{D} \right) \left[\frac{1 + (\tau_2/\tau_1)(1 + \zeta_2)e^{-\zeta_2} - (1 + \zeta_1)e^{-\zeta_1}}{1 + e^{-\zeta_2} - e^{-\zeta_1}} \right]^{1/2}, \quad (25)$$

$$\langle t \rangle = \tau_1 \left[\frac{1 + (\zeta_1 + \tau_2/\tau_1)e^{-\zeta_2} - (1 + \zeta_1)e^{-\zeta_1}}{1 + e^{-\zeta_2} - e^{-\zeta_1}} \right], \quad (26)$$

where

$$\tau_{1,2} = c^{-1} D_s' \sigma_{d1,2}^2 \quad (27)$$

$$\zeta_1 = \frac{1}{2} \left[\frac{X_1}{D_s' \sigma_{d1}} \right]^2 \quad (28)$$

$$\zeta_2 = \frac{\tau_1}{\tau_2} \zeta_1, \quad (29)$$

and $\sigma_{d1,2}$ is the rms scattering angle produced by each screen.

Figure 2 shows θ_{rms} plotted against frequency for different ratios, σ_{d1}/σ_{d2} and assuming that $\sigma_{d1,2} \propto \nu^{-2}$. The figure demonstrates how the weaker first component dominates the apparent source size at high frequencies and the second at low frequencies, with a plateau where the angular size is nearly independent of frequency.

Figure 3 shows a similar plot, now for the mean pulse broadening time, $\langle t \rangle$, plotted against frequency for different ratios, t_2/t_1 , and assuming that $\sigma_{d1,2} \propto \nu^{-2}$. The figure demonstrates how the weaker first component dominates pulse broadening at high frequencies and the second at low frequencies, with a plateau where the pulse broadening is nearly independent of frequency.

4.2. Scattering from Filaments

Figure 4 shows scattering from a filament located along the direct ray path for three values of rms scattering angle in the filament. Small rms scattering yields a circular image and an exponential pulse broadening function. For sufficiently large scattering angles, the image becomes elongated and tends toward a $t^{-1/2}e^{-t}$ pulse broadening function

Figure 5 shows scattering from a filament at different locations relative to the direct ray path but for identical rms scattering angles in the filament. When the filament is near enough to the image center, the pulse broadening function is bimodal. When the filament is far, the pulse broadening function is dominated by the much weaker scattering from outside the filament. The broadening component from the filament is delayed by a time related to the offset of the filament from the direct ray. Clearly, a superposition of filaments near the direct ray would produce a multiplicity of pulses. We explore this result further in a separate paper to discuss giant pulses from the Crab pulsar.

Figure 6 shows scattering from an ensemble of filaments at different frequencies. As can be seen, the pulse broadening function shows multiple peaks that align at different frequencies. The number of filaments that are ‘lit up’ by the scattering decreases in going to higher frequency.

5. Application to Galactic Scattering: Crab Pulsar, NGC 6334B, Cygnus X-3, & Sgr A*

Galactic sources show a wide range of scattering levels, indicative of the concentration of intense scattering into a Population I type Galactic distribution (Cordes et al. 1985; Taylor & Cordes 1993).

Here we discuss particular objects whose scattering may be interpreted in the context of this paper’s formalism. Our discussion is brief. We defer to separate articles any detailed treatment on particular sources.

5.1. The Crab Pulsar

The Crab pulsar shows enhanced pulse broadening from nebular material that has been recognized since shortly after the pulsar’s discovery in 1968 (e.g., Vandenburg 1976 and references therein). The nebular contribution is highly episodic, with dramatic increases of the pulse broadening time by a factor of 100 (Lyne & Thorne 1975; Isaacman & Rankin 1977). Recently, multiple images have been inferred from the presence of echoes of the pulse shape (Graham Smith & Lyne 2000; Backer 2000).

Giant pulses from the Crab pulsar show additional evidence for nebular contributions to the scattering that are probably from discrete filaments. At relatively high frequencies (1.4 to 5 GHz), giant pulses show multiple pulse components that tend to have exponential scattering tails with time constants that often differ, even within the same spin period of the pulsar (Hankins & Moffett 1998; Sallmen et al. 1999; Hankins 2000). Also, the widths of the pulse components appear to scale less strongly with frequency than ν^{-2} . These characteristics suggest consistency with the overall picture developed in this paper. A detailed analysis of the Crab pulsar’s pulses is deferred to another paper.

5.2. NGC 6634B

The largest angular broadening measured is for the extragalactic source NGC 6634B viewed through the H II complex NGC 6334 (Trotter, Moran, & Rodríguez 1998 and references therein), $\theta_d \approx 3''$ at 1.4 GHz. The image’s position angle rotates in going from low to high frequency, and the image axial ratio may increase from 1.2 at 1.4 and 5 GHz to 1.5 at 15 GHz. Trotter et al. (1998) interpret this variation as signifying an outer scale for the wavenumber spectrum of *anisotropically-scattering* density irregularities, $\ell_{out} \lesssim 10^{16}$ cm. This proposed outer scale is comparable to the thickness of the H II shell in this region (Rodríguez, Canto, & Moran 1988; Kahn & Breitschwerdt 1990). An alternate possibility is that the density irregularities scatter isotropically, but that the anisotropic images reflect density irregularities that are confined to the H II shell.

If the latter were the case, we would expect that the axial ratio would increase as a function of decreasing frequency. At lower frequencies, the size of the minor axis of the scattering diameter would be constrained by the width of the H II shell while the size of the major axis would be essentially unconstrained, unless the scattering is so intense that the size of the major axis is also limited by the scale of the H II shell. For NGC 6634B, the axial ratio appears to be constant with frequency or increasing with increasing frequency. The frequency behavior of the axial ratio

indicates that any relevant length scales in the H II shell must be smaller than 10^{14} cm (the smallest length scale probed by the highest frequency observations) or larger than 10^{17} cm (the largest length scale probed by the lowest frequency observations).

5.3. Cygnus X-3

The compact source Cyg X-3 is heavily scattered ($0''.5$ at 1 GHz) and has an anisotropic image (axial ratio ≈ 1.2 and increasing with increasing frequency) whose position angle varies with frequency (Wilkinson, Narayan, & Spencer 1994; Molnar et al. 1995). The variation of position angle has been interpreted by Wilkinson et al. (1994) as due to a changing orientation of diffracting irregularities on a length scale of order $\theta(D - D_s) \sim 0.01$ pc. In their picture, the image asymmetry is due to anisotropic diffracting irregularities, and the orientation change with frequency is attributed to the spatial variation of those irregularities.

An alternative explanation is that the diffracting irregularities are isotropic and that the image anisotropy reflects spatial variations of the strength of the diffracting irregularities on the scale $\theta(D - D_s)$. Molnar et al. (1995) have proposed that the H II region DR 11 is responsible for the bulk of the scattering along this line of sight. A key difficulty with this explanation is that the axial ratio increases with increasing frequency. This is inconsistent with the notion of scattering from a single filament but may be consistent with scattering from a group of filaments which are individually smaller than 10^{16} cm.

5.4. Sgr A* & Galactic-Center OH/IR Masers

Galactic center sources show large scattering diameters ($\sim 1''$ at 1 GHz) and significant image asymmetries that vary across the roughly $30'$ size of the scattering region (Lazio & Cordes 1998). The major axis of the image of Sgr A* shows a ν^{-2} frequency dependence from 1.4 to 22 GHz (Yusef-Zadeh et al. 1994; Lo et al. 1998), and the image itself displays no change in its major axis, axial ratio, or orientation on time scales as long as a decade (Lo et al. 1998; Marcaide et al. 1999).

Deviations from a ν^{-2} dependence for the major axis, minor axis, or both are claimed at a variety of frequencies from as low as 43 GHz (Lo et al. 1998) to as high as 215 GHz (Krichbaum et al. 1998). These deviations from the ν^{-2} dependence observed at lower frequencies are commonly interpreted as an effect of the intrinsic source diameter becoming important at the various frequencies.

The deviations could also be symptomatic of the size scale of the scattering medium. If this is the case, then the frequencies at which the breaks occur correspond to spatial scales $\ell \sim 5$ AU (for a break occurring at 43 GHz) to as small as 0.17 AU (at 215 GHz). These spatial scales are comparable to the outer scale inferred by Lazio & Cordes (1998), on the basis of a comparison of

scattering strength and thermal free-free emission. However, the velocities in the Galactic center ($\sim 50 \text{ km s}^{-1}$) suggest that variations in the orientation of the image of Sgr A* should be seen on timescales of order $0.1 \text{ yr}(\ell/1 \text{ AU})(v/50 \text{ km s}^{-1})^{-1}$. As mentioned above, these are not seen. This implies either that all striations in the medium are oriented in the same direction or that the intrinsic source size is in fact important at high frequencies.

The lack of variations in the image orientation indicates that there are not likely to be striations or other structure in the scattering screen on scales smaller than about 1 AU. Variations do occur, though, on much larger scales, of order $15'$ corresponding to spatial scales of roughly 25 pc, the separations between Sgr A*, the various OH masers, and other scattered sources (Lazio et al. 1999). Effects from the spatially-limited scattering described in this paper are unlikely to be seen with the current census of Galactic center sources. The narrowband nature of OH masers means that the wavelength dependence of their scattering diameters cannot be measured, and Sgr A* itself is obscured below 1 GHz due to free-free absorption by Sgr A. Detection of additional radio transients (e.g., Zhao et al. 1992) or radio pulsars (Cordes & Lazio 1997) may allow such effects to be detected at frequencies below 1 GHz.

5.5. Extreme Scattering Events

“Extreme scattering events” (ESE’s) are events identified in the light curves of several AGN’s (Fiedler et al. 1987, 1994) and two pulsars (Cognard et al. 1993; Maitia, Lestrade, & Cognard 1999). They are roughly consistent with *refractive* defocusing and caustic formation from discrete, small scale plasma structures (Fiedler et al. 1987; Romani et al. 1987; Clegg et al. 1998). However, alternative explanations invoke the outer ionized regions of predominantly neutral, primordial HI clouds (Walker & Wardle 1998) or distributed fluctuations much like those that account for the diffractive scintillations of pulsars (Fiedler et al. 1994). The fundamental difference between these models is the implied gas pressure. As discussed further below, a discrete structure is necessarily overpressured compared to the general ISM, so any such structures must exist either transiently or in regions of small volume filling factor that can support such pressure.

If ESEs result from discrete ionized structures, then effects described in this paper should be present in the scattered image and pulse shape (for pulsars). This notion is little explored because few ESEs have been identified and, given that most are seen from AGN’s, intrinsic source size effects can also diminish the appearance of diffraction effects. VLBI observations of the source 1741–038 undergoing an ESE have shown no indication of a truncated image (Lazio et al. 2000), however, those observations were at relatively high frequencies ($\geq 1.7 \text{ GHz}$) and had limited dynamic range. Pulse timing observations of PSR B1937+21 (Cognard et al. 1997) show no change in the pulse shape, though, again these observations were obtained at 1.4 GHz. Future observations of a source undergoing an ESE at lower frequencies (e.g., 0.33, 0.41, or 0.61 GHz) would place much more stringent constraints on the notion that ESEs arise from discrete ionized structures.

6. Future Observations

6.1. Extragalactic Scattering

Scattering from extragalactic plasma can arise from the distributed intergalactic medium (IGM), most of which is expected to be ionized, from intervening Ly- α clouds, and from intervening galaxies. Of greatest relevance to this paper are the last two cases and, of these, intervening galaxies are likely to be the more important because of their greater column densities. A face-on galaxy like the Milky way will scatter radiation from a background source into an apparent size of at least $\theta_d \sim 1 (\nu/0.33 \text{ GHz})^{-2.2}$ mas (Cordes & Lazio 1991; Taylor & Cordes 1993). Scattering by H II regions yields even larger angles, so some background sources, albeit at low-probability alignments, will display images that reflect the sizes of H II regions and, in some instances, spiral arms that contain them.

Scattering from an edge-on galaxy will be about 10^3 – 10^4 times larger, or $1''$ – $10''$ at 0.3 GHz. The lateral scale is $\theta_d D \sim 15$ – $150 \times D_{3000}$ kpc for $D = 3000 D_{3000}$ Mpc. Thus, near edge-on galaxies will produce scattered images that, in part, display the shapes of the galaxies. At even lower frequencies, scattering diameters from Lyman- α clouds and galaxies with significantly smaller scattering strength will produce similar effects. Imaging radio observations at ~ 0.1 GHz will thus probe intergalactic structures.

We defer to another paper a thorough discussion of intergalactic scattering, taking into account cosmological expansion and evolution. Scattering may be able to probe the intergalactic medium at redshifts near the reionization epoch.

6.2. Low-Frequency Galactic Observations

The (nominally) strong frequency dependence of interstellar scattering observables suggest that the anomalous scattering described here will most likely occur at low frequencies. High-resolution, low-frequency instruments such as the Giant Metrewave Radio Telescope (GMRT, Ananthakrishnan 1995) and the proposed Low Frequency Array (LOFAR, Kassim et al. 2000) and the low-frequency Square Kilometer Array (SKA, Butcher 2000) have or will have subarcminute resolution at frequencies below 150 MHz. Consequently, they may detect anomalous scattering along lines of sight less heavily scattered than those described in §5. Here we consider relevant lines of sight and frequencies for which anomalous scattering is a possibility.

The relevant length scale in regions of less intense scattering may be the outer scale of the density fluctuation spectrum ℓ_0 . (This may also be the relevant length scale in intense regions, though its value could be quite different.) Near the Sun (within ≈ 1 kpc), $l_0 \sim 1$ pc (Armstrong, Rickett, & Spangler 1995). It is unlikely scattering diameters will probe this spatial scale (i.e., $\theta_d D \sim \ell_0$) unless $\nu < 10$ MHz. As the ionosphere becomes increasingly opaque at frequencies $\nu < 10$ MHz, ground-based interferometric arrays will likely not be affected by anomalous scattering

in the solar neighborhood.

Toward the inner Galaxy, Galactic longitudes $|\ell| < 50$ deg, stronger scattering than that in the solar neighborhood (but still weaker than the intense scattering described in §5) will obtain. In this case, observations at meter wavelengths may display anomalous scattering.

A competing effect for detecting anomalous scattering is free-free absorption. The density fluctuations responsible for interstellar scattering also contribute to free-free absorption. Sources seen along heavily scattered lines of sight at shorter wavelengths may be free-free absorbed at longer wavelengths. For instance, free-free absorption renders the Galactic center increasingly opaque for frequencies $\nu < 1$ GHz (Ananthramaiah et al. 1991).

7. Implications for the Interstellar Medium

As alluded to before, the existence of compact, turbulence-containing ionized structures is directly related to their longevity and rarity, or filling factor, in the Galaxy. Except for chance fluctuations from distributed turbulence, many observed phenomena suggest the existence of compact structures with densities that imply they are overpressured compared to most of the ISM. This is not overly surprising because the ISM is highly dynamic and is in pressure equilibrium only in some average sense. It is not known which kinds of locales (H II regions, supernova shocks, etc.) provide the largest scattering strengths. We suggest, simply, that the observable effects described in this paper might be used to better probe the physical sizes of regions that produce the largest levels of scattering.

Striations in interstellar gas densities on a host of length scales are most likely associated with magnetic fields. On diffraction scales $\lesssim 10^{11}$ cm, a compelling idea is that turbulence is essentially one dimensional and that irregularities are elongated along the field lines (Higdon 1984, 1986; Goldreich & Sridhar 1995). Larger scale filaments, such as those seen near the Galactic center perpendicular to the plane of the Galaxy (Yusef-Zadeh & Morris 1987), are also thought to be along the local field direction. If diffracting irregularities are contained in screens that are themselves elongated in the same direction, it may be difficult to separate (and thus identify) the two possible contributions to image elongation.

The frequency dependence of anomalous scattering may offer a means for identifying the cause of image elongation for a particular source if it is heavily scattered by a single (or few) filament(s). (cf. Figure 2 and §5). If the image elongation arises from anisotropic scattering by small-scale density irregularities, increased angular resolution should yield increased axial ratios as less spatial averaging is done over the small-scale irregularities. Conversely, if isotropic scattering from filaments causes image elongation, increased angular resolution should yield little or no change in the minor axis of the scattering disk (provided that the resolution is sufficient to resolve the scattering disk). A more complicated wavelength dependence may result if the scattering results from a number of smaller filaments.

The wavenumber spectrum of electron density irregularities is often constrained by the scaling law of angular size and pulse broadening (and its reciprocal, the scintillation bandwidth) with frequency. For moderate scattering, where the dominant length scales are between the inner and outer scales, the pulse broadening time scales as ν^{-x} with $x = -2\beta/(\beta-2)$, where β is the exponent of the three dimensional, isotropic wavenumber spectrum (Cordes et al. 1985; Rickett 1990). For a Kolmogorov spectrum, $\beta = 11/3$ and $x = 4.4$. If irregularities are isotropic, so that $\beta = 11/3$, but the medium is confined in the transverse direction, the actual value of x is lessened. The value of β inferred would be greater than $11/3$ in this instance. A similar trend occurs when angular broadening is used to infer β . It is not clear which, if any, of the published constraints on β are affected by the influence of scattering-region confinement. A detailed study of the wavenumber spectrum is deferred to another paper.

8. Summary

In this paper we have shown that radio scattering observables such as image shapes and pulse broadening functions can be strongly influenced by structure in the scattering medium on length scales substantially larger than those that cause the scattering. As such, careful multifrequency observations can be used to constrain properties of the interstellar medium on scales that are typically $\sim 1\text{--}10$ AU. Intergalactic scattering has not been identified but is certainly expected from intervening spiral galaxies, probably expected for some Lyman- α clouds, and may occur from distributed ionized gas. For intergalactic scattering, relevant length scales can be comparable to the sizes of galaxies. A low-frequency VLBI survey of extragalactic sources may thus probe the level of scattering in other galaxies and in the general intergalactic medium. It is also expected that scattering of radiation from gamma-ray burst afterglows will be influenced in some cases by intervening ionized gas in the IGM as well as in the Milky Way's ISM. These issues will be explored in separate articles.

We thank B. Rickett for helpful discussions. This work was supported by NSF Grant AST 9819931 to Cornell University. Basic research in radio astronomy at the NRL is supported by the Office of Naval Research.

REFERENCES

Ananthakrishnan, S. 1995, JApAS, 16, 427

Anantharamaiah, K. R., Pedlar, A., Ekers, R. D., & Goss, W. M. 1991, MNRAS, 249, 262

Armstrong, J. W., Rickett, B. J., & Spangler, S. R. 1995, ApJ443, 209

Backer, D. C. 2000, in Pulsar Astronomy—2000 and Beyond, IAU Colloquium 177, eds. M. Kramer, N. Wex, & R. Wielebinski (ASP: San Francisco) p. 499

Bower, G. C. & Backer, D. C. 1998, *ApJ*, 496, L97

Butcher, H. R. 2000, in *Radio Telescopes*, ed. H. R. Butcher (SPIE) in press

Clegg, A. W., Fey, A. L., & Lazio, T. J. W. 1998, *ApJ*, 496, 253

Cognard, I., et al. 1993, *Nature*, 366, 320

Cordes, J. M., Weisberg, J. M., & Boriakoff, V. 1985, *ApJ*, 288, 221

Cordes, J. M., & Lazio, T. J. 1991, *ApJ*, 376, 123

Cordes, J. M. & Lazio, T. J. W. 1997, *ApJ*, 475, 557

Cordes, J. M. & Rickett, B. J. 1998, *ApJ*, 507, 846

Fey, A. L., Spangler, S. R., & Cordes, J. M. 1991, *ApJ*, 372, 132

Fiedler, R. L., Dennison, B., Johnston, K. J., & Hewish, A. 1987, *Nature*, 326, 675

Fiedler, R. L., Dennison, B., Johnston, K. J., Waltman, E. B., & Simon, R. S. 1994, *ApJ*, 430, 581

Goldreich, P. & Sridhar, S. 1995, *ApJ*, 438, 763

Graham Smith, F. & Lyne, A. G. 2000, in *Pulsar Astronomy—2000 and Beyond*, IAU Colloquium 177, eds. M. Kramer, N. Wex, & R. Wielebinski (ASP: San Francisco) p. 503

Hankins, T. H. 2000, in *Pulsar Astronomy—2000 and Beyond*, IAU Colloquium 177, eds. M. Kramer, N. Wex, & R. Wielebinski (ASP: San Francisco) p. 165

Hankins, T. H. & Moffett, D. A. 1998, *Bull. A.A.S.*, 192, 570.

Higdon, J. C. 1986, *ApJ*, 309, 342

Higdon, J. C. 1984, *ApJ*, 285, 109

Isaacman, R. & Rankin, J. M. 1977, *ApJ*, 214, 214.

Kahn, F. & Breitschwerdt, D. 1990, *MNRAS*, 242, 209

Kassim, N. E., Lazio, T. J. W., Erickson, W. C., Crane, P. C., Perley, R. A., & Hicks, B. 2000, in *Radio Telescopes*, ed. H. R. Butcher (SPIE) in press

Krichbaum, T. P., et al. 1998, *A&A*, 335, L106

Lambert, H. C. & Rickett, B. J. 1999, *ApJ*, 517, 299

Lazio, T.J.W. & Cordes, J. M. 1998, *ApJ*, 505, 715

Lazio, T. J. W., Anantharamaiah, K. R., Goss, W. M., Kassim, N. E., & Cordes, J. M. 1999, *ApJ*, 515, 196

Lazio, T. J. W., et al. 2000, *ApJ*, 534, 706

Lo, K. Y., Shen, Z.-Q., Zhao, J.-H., & Ho, P. T. P. 1998, *ApJ*, 508, L61

Lyne, A. G., & Thorne, D. J. 1975, *MNRAS*, 172, 97.

Lyutikov, M. & Parkih, A. 2000, in *Pulsar Astronomy—2000 and Beyond*, IAU Colloquium 177, eds. M. Kramer, N. Wex, & R. Wielebinski (ASP: San Francisco) p. 393

Maitia, M., Lestrade, J.-F., & Cognard, I. 1999, *ApJ*, submitted

Marcaide, J. M., Alberdi, A., Lara, L., Perez-Torres, M. A., & Diamond, P. J. 1999, *A&A*, 343, 801

Molnar, L. A., Mutel, R. L., Reid, M. J., & Johnston, K. J. 1995, *ApJ*, 438, 708.

Rickett, B. J. 1990, *ARA&A*, 28, 561.

Rodríguez, L. F., Canto, J., & Moran, J. M. 1988, *ApJ*, 333, 801

Scheuer, P. A. G. 1968, *Nature*, 218, 920

Sallmen, S., Backer, D. C., Hankins, T. H. & Lundgren, S. 1999, *ApJ*, 517, 460

Taylor, J. H. & Cordes, J. M. 1993, *ApJ*, 411, 674 (TC93)

Trotter, A. S., Moran, J. M. & Rodriguez, L. F. 1998, *ApJ*,

Vandenberg, N. R. 1976, *ApJ*, 209, 578

Walker, M. & Wardle, M. 1998, *ApJ*, 498, 125

Wilkinson, P. N., Narayan, R., & Spencer, R. E. 1994, *MNRAS*, 269, 67

Williamson, I. P. 1972, *MNRAS*, 157, 55

Williamson, I. P. 1973, *MNRAS*, 163, 345

Williamson, I. P. 1975, *Proc. R. Soc. Lond. A.*, 342, 131

Yusef-Zadeh, F. & Morris, M. 1987, *ApJ*, 320, 545

Zhao, J., et al. 1992, *Science*, 255, 1538

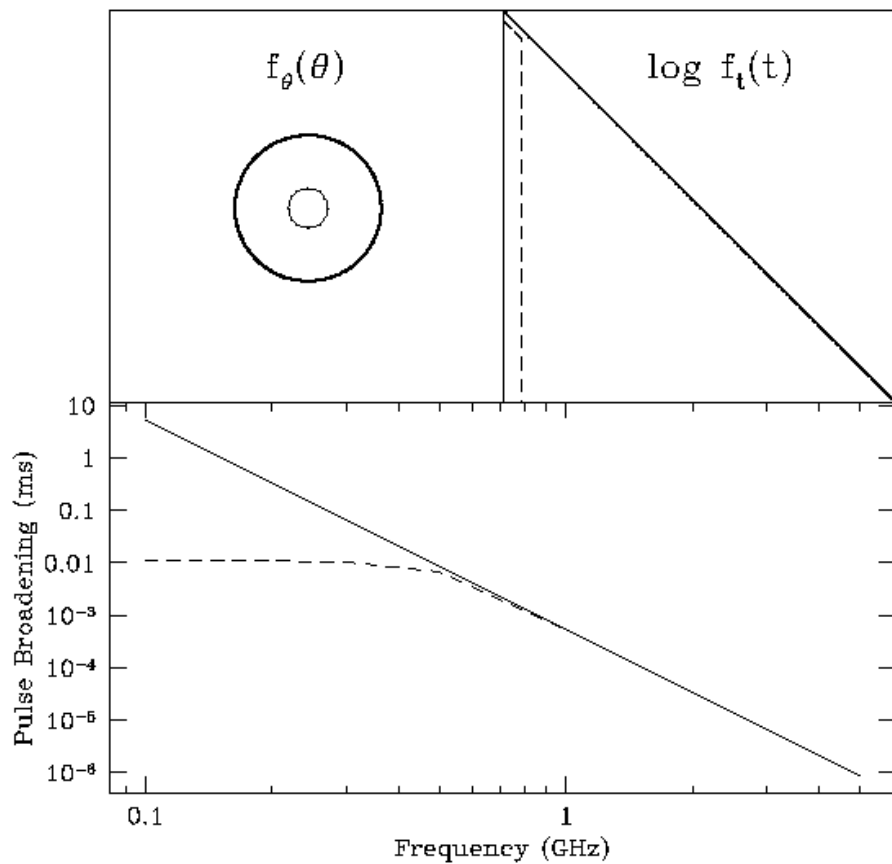


Fig. 1.— Scattering from an infinite screen (heavy solid lines) and from a truncated circular screen centered on the direct line of sight (light and dashed lines). Top left panel: image contours at half-width at half maximum. Top right panel: pulse broadening functions. Bottom panel: pulse broadening time vs. frequency.

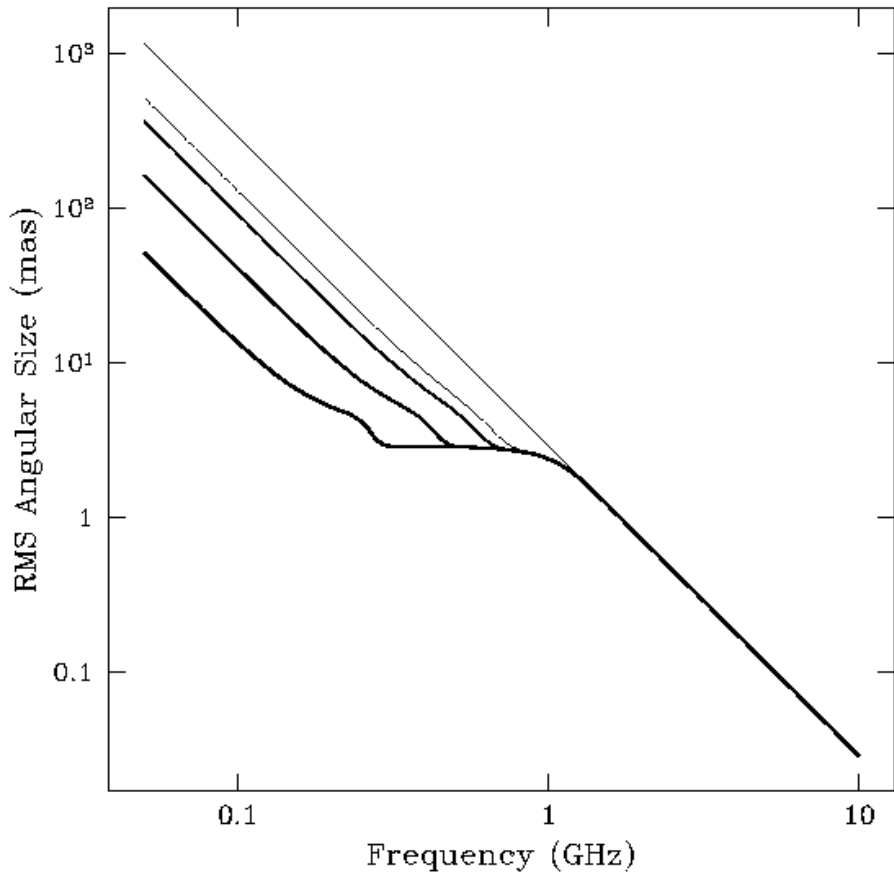


Fig. 2.— RMS angular size plotted against frequency for a two component scattering screen, with a strongly scattering central part and a more weakly scattering extended part. The curves correspond to different ratios, $\sigma_2/\sigma_1 = 500, 50, 10, 5, 1$ in order of thickest to thinnest lines, where σ_1 is the rms scattering angle from the central part and σ_2 is the value for the extended part.

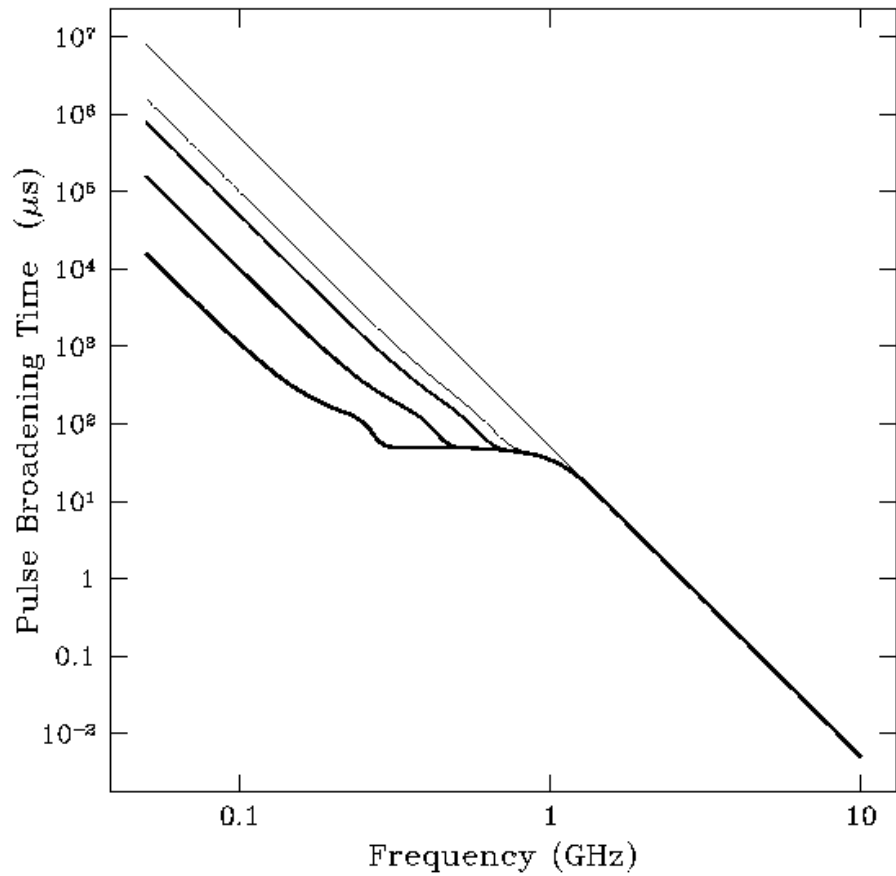


Fig. 3.— Pulse broadening time plotted against frequency for a two component scattering screen, with a strongly scattering central part and a more weakly scattering extended part. The curves correspond to different ratios, $\tau_c/\tau_e = 500, 50, 10, 5, 1$ in order of thickest to thinnest lines, where τ_c is the pulse broadening time of the central part (if it were infinite in extent), and τ_e is the value for the extended part.

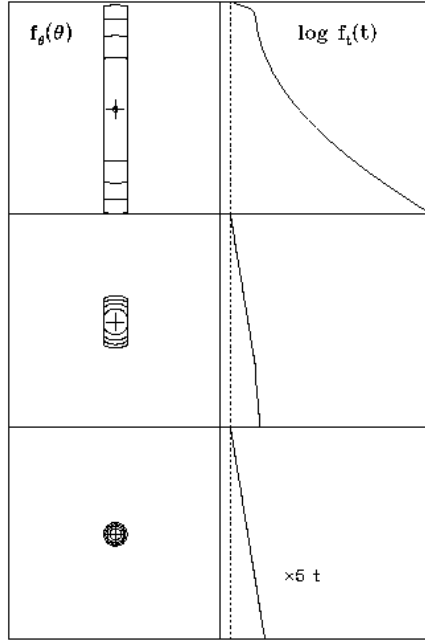


Fig. 4.— Images and pulse broadening functions for a vertical filament along the direct line of sight but with different rms scattering angles. The filament has a width of $0''.3$, and the rms scattering angle is $1''$, $0''.25$, and $0''.11$ going from the top to the bottom frame. The contour levels extend from the maximum down to 10^{-3} of the maximum in uniformly spaced intervals in the log. The pulse broadening function is also shown on a log-linear scale with 3 orders of magnitude on the vertical axis. Top: large rms scattering angle so that the image shape is dominated by the edges of the filament. The pulse broadening function is nearly of the form $t^{-1/2}e^{-t}$. Middle: smaller rms scattering angle so that the image is less elongated. The pulse broadening function is intermediate between $t^{-1/2}e^{-t}$ and e^{-t} . Bottom: rms scattering angle small enough so that the edges of the filament are not seen. The pulse broadening function is exponential in form, e^{-t} . In the bottom right frame, the time axis has been expanded by a factor of 5 relative to the frames above it.

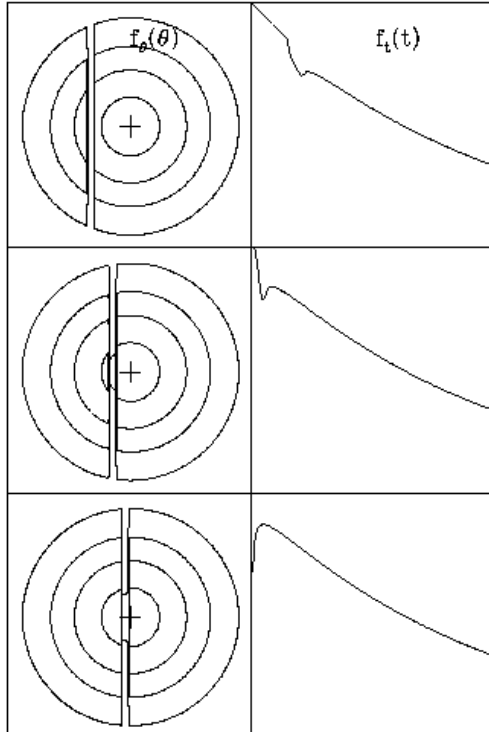


Fig. 5.— Images and pulse broadening functions for a filament at different locations from the direct line of sight. Screen locations outside the filament have an rms scattering angle that is 0.1 of that in the filament. (Top) The image is a circular Gaussian combined with a much weaker subimage from the filament. The pulse broadening function (displayed over 3 orders of magnitude) is exponential in form, $\propto e^{-t}$. (Middle) The filament is close enough so that its subimage now contributes significantly to the pulse broadening function, which is bimodal. (Bottom) The circular and filamentary subimages are partially merged and the pulse broadening function is now much wider.

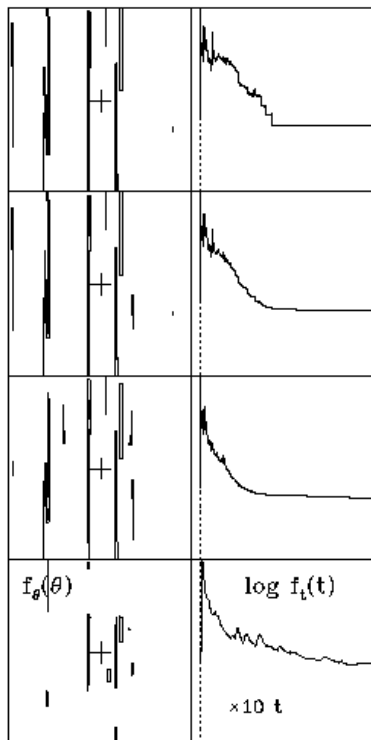


Fig. 6.— Images and pulse broadening functions for an ensemble of filaments superposed combined with a much stronger scattering screen. The filaments therefore represent “gaps” where the scattering is weaker than in the screen, but still strong enough to scatter radiation back to the observer. The screen has rms scattering angle of 2 mas while the filaments have scattering between 0.1 and 2 mas. From top to bottom, $\nu = 0.1, 0.2, 0.3$, and 0.5 GHz.